

Self-Organized Vortices of Circling Self-Propelled Particles and Curved Active Flagella

Yingzi Yang and Feng Qiu

*The State Key Laboratory of Molecular Engineering of Polymers,
Department of Macromolecular Science, Fudan University, Shanghai 200433, China*

Gerhard Gompper

*Theoretical Soft Matter and Biophysics, Institute of Complex Systems and Institute
for Advanced Simulation, Forschungszentrum Jülich, D-52425 Jülich, Germany*

Self-propelled point-like particles move along circular trajectories when their translocation velocity is constant and the angular velocity related to their orientation vector is also constant. We investigate the collective behavior of ensembles of such circle swimmers by Brownian dynamics simulations. If the particles interact via a “velocity-trajectory coordination” rule within neighboring particles, a self-organized vortex pattern emerges. This vortex pattern is characterized by its particle-density correlation function G_ρ , the density correlation function G_c of trajectory centers, and an order parameter S representing the degree of the aggregation of the particles. Here, we systematically vary the system parameters, such as the particle density and the interaction range, in order to reveal the transition of the system from a light-vortex-dominated to heavy-vortex-dominated state, where vortices contain mainly a single and many self-propelled particles, respectively. We also study a semi-dilute solution of curved, sinusoidal-beating flagella, as an example of circling self-propelled particles with explicit propulsion mechanism and excluded-volume interactions. Our simulation results are compared with previous experimental results for the vortices in sea-urchin sperm solutions near a wall. The properties of the vortices in simulations and experiments are found to agree quantitatively.

I. INTRODUCTION

Systems of self-propelled particles (SPPs), which consume energy to maintain a persistent non-Brownian motion, exhibit an abundance of fascinating non-equilibrium collective behaviors — such as swarming, swirling, and clustering [1]. Examples are found in very different areas of physics and biology, and range from actin filaments in motility assays [2, 3] through metallic nano-rods [4, 5] to flocking of birds [6, 7] and groups of people [8, 9]. In all of these examples, SPPs employ different propulsion mechanisms, and also interact with each other in different ways, including direct physical contact [10, 11], chemotaxis [12], hydrodynamic interactions [13–15], and restricted visual contact [16]. However, the collective behavior of SPPs systems is surprisingly similar, displaying phenomena such as giant density fluctuations with anomalously slow relaxation [17–19], order-disorder phase transition with increasing noise and decreasing density [20–25], etc.

Since the simplest model of interacting SPPs was introduced by Vicsek et al. [20], nowadays widely referred as the “Vicsek model” [21–26], collective behavior of SPP systems has attracted much interest [1]. In the Vicsek model, point par-

ticles moving with constant velocity align their directions of motion with the average direction of other particles in a prescribed interaction range, while internal or external noise is taken into account by adding a random increment to their orientation vectors. By a variation of the system parameters, e.g. the particle density and the strength of the perturbation, such a simple system has been found to undergo an order-disorder phase transition, whose nature (first or second order) is related to the particle velocity and the way the perturbation is introduced [21, 27, 28]. According to these studies, the initial conditions and settings of the simulation, the type of interaction and the boundary conditions play an important role in the formation of certain collective patterns of motion [1].

A special, but not rare class of patterns of collective motion in SPPs systems are swirls or vortices, in which a group of particles circle around a common center. In experiments, swirls and vortices emerge both in non-living particle systems (vertically vibrated granular rods [29], actin filaments in motility assays [2]) and in systems of living micro-organisms (bacteria colonies [12], zoo-plankton under optical stimulus [30], sea-urchin sperm trapped near a substrate [31]). In simulations, the emergence of swirls and vortices was found to depend on the initial conditions and the model settings, such

as a circular boundary [32, 33], alignment with a “blind angle” of interaction behind each agent [16], a harmonic attractive pair potential with a noise above a critical value [34], and hydrodynamic interactions [13]. In most of the computational models exhibiting vortices, a single SPP is either assumed to perform a random walk [30], or to move with constant magnitude of velocity [12, 16, 32, 34].

In this paper, we consider a class of SPPs which move — in the absence of noise — along *curved trajectories* rather than straight lines, which we call circle SPPs. The driving force of a circle SPP does not coincide with its propagation direction, so that its trajectory is a cycloid in three spatial dimensions or a circle in two dimensions [35–37]. Artificial circle swimmers can be constructed by introducing a tilted or bend structure to catalytically driven colloidal rods [5], giving thermophoretic colloidal swimmers a L-shape [38], or by designing micro-machines of connected beads which are moved relative to each other in a time-irreversible multi-step cycle [39]. Examples of circle swimmers in living systems include certain bacteria [40] and spermatozoa [31, 41, 42] — when the micro-organisms are attracted or confined in their motion to a surface or wall. The most carefully analyzed experiment on the collective motion of circle SPPs might be the self-organized vortices of sea-urchin sperm [31]. The 50- μm -long sperm circle clockwise when they gather at a substrate. With increasing surface density of sperm, the system exhibits a transition from a disordered state of randomly distributed sperm to a self-organized vortex-array state with local hexagonal order, in which each vortex consists of several sperm. In Ref. 31, the emergence of this structure is attributed to the hydrodynamic interactions between individual sperm and between sperm vortices. However, simulations suggest that the steric interactions between rod-like SPPs [10, 11] and sinusoidal beating flagella [11] strongly contribute to the collective motion and aggregation.

While the morphology and properties of swirls and vortices in straight-trajectory SPPs systems have been studied intensively in recent years [12, 13, 16, 32–34], much less is known theoretically about the collective motion of circle SPPs. The understanding of the effect of the spontaneous circular trajectory on the collective behavior of SPPs is essential for the understanding of many biological phenomena and for the design of microscopic machines. In addition to the parameters of SPPs (like velocity, particle density, interaction range, and noise amplitude), the circle SPP systems have at

least the spontaneous curvature of the particle trajectory as an extra parameter. The larger parameter space suggests a more complex behavior of these systems. In order to study such systems, highly simplified models are often very useful, as has been demonstrated by the success of the Vicsek model. An example for circle swimmers is the simplified model of Ref. 31, designed to interpret the formation of vortex arrays of sea urchin sperm. In this model, each sperm is described by a point particle at its trajectory center, with a pairwise short-range attraction arising from hydrodynamic forces, and a longer range repulsion due to steric or hydrodynamic origin. Inspired by this model, we construct a model of circle SPPs by point-like particles with a constant propagation velocity, where particles interact through a “velocity-trajectory coordination”, which takes the trajectory centers of neighbor particles into account. This algorithm of interaction is different from both the “trajectory-center coordination” of Ref. 31 and the “velocity coordination” of the Vicsek model [20] (which averages the velocity of neighboring particles). We will analyze this model in detail, and show that it describes vortex formation and the evolution of a stationary vortex pattern.

In addition to the point-like circle SPPs model, we also study curved, sinusoidal-beating flagella. Sinusoidal beating of a filament or elongated body is a common self-propulsion mechanism in biological systems with low-Reynolds-number hydrodynamics, e.g. nematodes [43] and sperm of higher animals [44, 45]. The sinusoidal wave propagates from one end to the other on the filament-like body and pushes the surrounding fluid backwards to generate a forward force. Thus, the cell or organism gains velocity in opposite direction of wave propagation. As indicated by experiments of biological systems [43, 46–48] and simulations of model systems [11], the sinusoidally undulating motion of the body does not destroy the general collective behaviors of rod-like SPPs. Our flagellum model is coarse-grained as particles connected by harmonic springs, and the hydrodynamics is either approximated by anisotropic friction, or calculated by using Multi-Particle Collision dynamics (MPC), a mesoscopic particle-based simulation approach [49, 50]. By introducing a non-zero average curvature in the beating plane, the undulating flagellum traces out a circular trajectory in two dimensions, reminiscent the trajectory of sea urchin sperm at a substrate [31, 51]. The simplicity of the model allows us to analyze the contribution of volume exclusion and hydrodynamic interaction separately. The study provides insight into the effect of flagellar proper-

ties, such as frequency distribution and spontaneous curvature, on the collective motion and the emerging vortex patterns.

The paper is organized as follows. Section II gives a brief description of our models and simulation methods. In Sec. III, we analyze the collective motion of point-like circle SPPs systems. Then, we study the collective motion of curved, sinusoidally beating flagella, and compare the results with circle SPPs models and sea-urchin sperm experiments in Sec. IV. The results are summarized in Sec. V.

II. MODELS

A. Circle self-propelled particles

We consider N point-like particles moving in a two-dimensional system of size $L_x \times L_y$. The number density of the particles is $\rho_0 = N/L_x L_y$. Each particle has a spontaneous circular trajectory of diameter D_0 , which is traversed in counter-clockwise direction, and a circular interaction region of diameter d , as illustrated in Fig. 1. At time t , the i -th particle has position \mathbf{r}_i , velocity \mathbf{v}_i , and trajectory center position $\mathbf{r}_{c,i}$ of its spontaneous circle trajectory determined by

$$\mathbf{r}_{c,i}(t) = \mathbf{r}_i(t) + \frac{D_0}{2} \mathfrak{R}\left(\frac{\pi}{2}\right) \frac{\mathbf{v}_i(t)}{|\mathbf{v}_i(t)|}, \quad (2.1)$$

where $\mathfrak{R}(\theta)$ is a rotation matrix which rotates a vector in two dimensions counter-clockwise through an angle θ . Note that $\mathbf{r}_{c,i}(t)$ is obtained from the instantaneous velocity and position, rather than from the full trajectory.

The equation of motion for the i -th particles is then given by

$$\mathbf{r}_i(t + \Delta t) = \mathbf{r}_i(t) + \mathbf{v}_i(t + \Delta t)\Delta t. \quad (2.2)$$

Motivated by the nematic alignment of colliding rod-like particles [25], we define a majority rule for the re-direction of the velocity as

$$\mathbf{v}_i(t + \Delta t) = v_0 \mathfrak{R}(\omega_0 \Delta t) \frac{\sum_{j(i)} \mathbf{e}_j}{|\sum_{j(i)} \mathbf{e}_j|}, \quad (2.3)$$

where Δt is the simulation time step, v_0 is constant magnitude of the velocity, $\omega_0 = \frac{2v_0}{D_0}$ is the angular velocity of the orientation of the particle velocity which enforces a circular trajectory of diameter D_0 in dilute suspension, and $\sum_{j(i)}$ is the sum of all particles within the interaction region of i -th particle – including i -th particle itself. The tangential unit vector

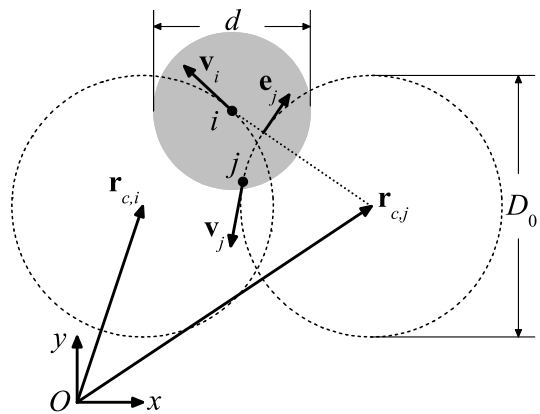


FIG. 1. Schematic of the interaction of particles i and j . The dashed lines denote the spontaneous circular trajectories of the i -th and j -th particles. The gray area displays the neighbor region of particle i . \mathbf{e}_j is the tangential unit vector to the trajectory of particle j with $\mathbf{v}_i \cdot \mathbf{e}_j \geq 0$.

\mathbf{e}_j is obtained at the intersection of the spontaneous trajectory of j -th particle and the connect line between \mathbf{r}_i and $\mathbf{r}_{c,j}$, as illustrated in Fig. 1. The direction of \mathbf{e}_j is chosen to make $\mathbf{v}_i \cdot \mathbf{e}_j \geq 0$.

In contrast to the Vicsek model [1, 20], the change of the velocity direction in our model is determined not by a polar alignment of velocities (velocity coordination), but rather by a nematic alignment of local trajectories, which are determined by the instantaneous trajectory centers $\mathbf{r}_{c,j}$ of the neighbor particles (velocity-trajectory coordination). Here, the choice of the alignment rule strongly depends on the interaction range relative to the preferred swimming radius. Clearly, a majority rule can only generate alignment if the number of particles in the interaction range is sufficiently large. This is very difficult to achieve for $d \ll D_0$ when particles move collective in circular vortices. Therefore, we choose $d \simeq D_0$. Our simulations show that in this case velocity coordination as in the Vicsek model does not give rise to vortex patterns in a circle SPP system, because neighboring particles align their directions of motion but do not tend to generate vortices with several particles circling around a common center.

Note that we omit noise terms in Eqs. (2.2) and (2.3), so that our model is deterministic – once the initial state is given. This is a reasonable description of microswimmers which are not too small, such as sperm.

In the simulation, we use the diameter of spontaneous trajectory D_0 as length unit, Δt as time unit, and $v_0 = 0.025D_0/\Delta t$. This implies a period of rotation of an

interaction-free particle of $T_0 = \pi D_0/v_0$. The interaction range d is varied below, but is typically on the order of D_0 (as explained above). The simulation box size is $L_x = L_y = 20D_0$ or $40D_0$. The simulation time for each system is $T = 5 \times 10^5 \Delta t \approx 4.0 \times 10^3 T_0$.

B. Circle-swimming flagella

We construct a two-dimensional flagellum model [15] from a linear sequence of N_f beads, which are connected by harmonic springs with rest length l_0 . The local spontaneous curvature of such a filament is a function of time t and position x along the flagellar contour, measured from the first bead,

$$c(x, t) = c_0 + A \sin(-2\pi f t + q x + \varphi_0), \quad (2.4)$$

where f is the beating frequency, q is the wave number, φ_0 is the initial phase chosen independently from a uniform distribution on the interval $[0, 2\pi)$ for each flagellum, and c_0 is the average curvature. We denote a flagellum with non-zero c_0 a curved flagellum. The constant A controls the strength of beating, which is related to the amplitude of the shape undulations. Equation (2.4) generates a traveling wave, which propagates from the front to the end of the flagellum. The curvature elasticity of the flagellum is determined by a bending potential, which depends on the deviations of the angles between neighbor bonds from their preferred value $c(x, t)l_0$. Therefore, the elastic energy of flagellum j is given by

$$V_j = \sum_{i=1}^{N_f-1} \frac{1}{2} \frac{k}{l_0^2} \left[|\mathbf{R}_{i,j}| - l_0 \right]^2 + \sum_{i=1}^{N_f-2} \frac{1}{2} \frac{\kappa}{l_0^3} \left[\mathbf{R}_{i+1,j} - \mathfrak{R}(c_j(x_i, t)l_0) \mathbf{R}_{i,j} \right]^2. \quad (2.5)$$

Here, $\mathbf{R}_{i,j} = \mathbf{r}_{i+1,j} - \mathbf{r}_{i,j}$ are bond vectors, and $\mathbf{r}_{i,j}$ denotes the position of the i -th bead of the j th flagellum. $\mathfrak{R}(c_j l_0)$ is an operator rotating a two-dimensional vector counter-clockwise by an angle $c_j(x_i, t)l_0$. k is the spring constant and κ the bending rigidity [52]. The volume exclusion of beads on different flagella is taken into account by a purely repulsive, truncated and shifted Lennard-Jones potential

$$V_{LJ}(r) = \begin{cases} 4\epsilon \left[\left(\frac{l_0}{r} \right)^{12} - \left(\frac{l_0}{r} \right)^6 + \frac{1}{4} \right], & r \leq 2^{1/6} l_0 \\ 0, & \text{otherwise} \end{cases}, \quad (2.6)$$

where r is the distance between two beads belonging to different flagella.

The swimming of both nematodes and sperm is determined by low-Reynolds-number hydrodynamics, where viscous forces dominate over inertial forces. In this regime, the dynamics of a rod can often be well described by resistive-force theory [44], in which hydrodynamic interactions between different segments of a rod are approximated by an anisotropic friction (AF), so that $\mathbf{f}_{\parallel} = -\gamma_{\parallel} \mathbf{v}_{\parallel} l_0$, $\mathbf{f}_{\perp} = -\gamma_{\perp} \mathbf{v}_{\perp} l_0$, where \mathbf{v}_{\parallel} and \mathbf{v}_{\perp} are the velocity components of a flagellum segment on the directions parallel and perpendicular to the local tangent vector, respectively. γ_B is the friction coefficient for a segment of unit length, with $B = \parallel$ or \perp [53]. Hydrodynamic interactions are not included in simulation employing AF, so that volume exclusion is the only interaction between the flagella in this case. Considering the relatively large sizes of flagella and nematodes of several $10 \mu\text{m}$ and a few millimeters, respectively, we neglect thermal fluctuations in our AF simulations.

In simulations with full hydrodynamics, the flagellum model is embedded in a two-dimensional fluid, and the time evolution of the system is carried out by employing a hybrid molecular dynamics approach — multi-particle collision dynamics (MPC) for the fluid [49, 50] in combination with molecular dynamics (MD) for the flagellum — as follows. During the streaming step, the point-like particles of the MPC fluid move ballistically during a time interval $\Delta\tau$, while Newton's equations of motion for the flagellum particles are integrated by the Verlet algorithm with a time step of $\Delta\tau' = 0.02\Delta\tau$. In the subsequent collision step, the flagella exchange momentum with the neighboring fluid particles. The collisions are performed by sorting all fluid and flagellum particles into the cells of a cubic lattice (with lattice constant a), which are labeled by an index ξ . A rotation operator $\mathfrak{R}_{\xi}(\alpha)$ is assigned to each box. If $\mathbf{v}_{c,\xi}$ is the pre-collisional center-of-mass velocity of all particles in box ξ , the post-collisional velocity \mathbf{v}'_i of a particle i in the box is given by $\mathbf{v}'_i = \mathbf{v}_{c,\xi} + \mathfrak{R}_{\xi}(\alpha) (\mathbf{v}_i - \mathbf{v}_{c,\xi})$, where \mathbf{v}_i is its pre-collision velocity. This simple collision rule conserves mass, momentum and energy, which guarantees the emergence of Navier-Stokes hydrodynamics on length scales larger than a . Since the beating flagella perpetually inject energy into the fluid, we apply a local thermostat after each collision step.

The simulation system contains N flagella of length $N_f l_0 = 50a$ in a simulation box of size $L_x \times L_y$, where a is size of a MPC collision box. The number density of flagellum is $\rho_0 = N/L_x L_y$. Periodic boundary conditions are em-

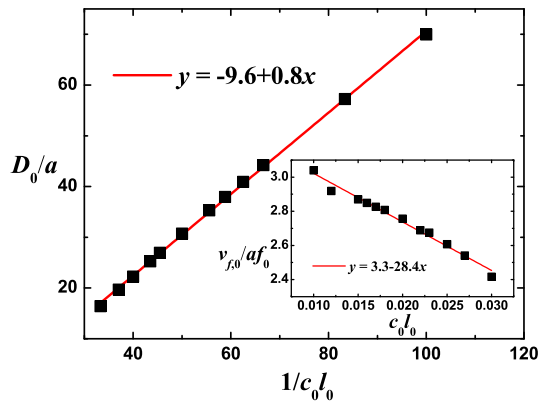


FIG. 2. (Color online) The diameter D_0 (black solid squares) of the circular trajectory of a single flagellum as a function of $(c_0 l_0)^{-1}$ in AF simulations. The red line is a linear fit to the data with slope of 0.8. The inset is the dimensionless velocity $v_0/f_0 a$ of a single flagellum (black solid squares) as a function of $c_0 l_0$. The red line is the linear fit to the data. In both (a) and (b), the beating frequency of the flagellum is $f_0 = 1/120\tau_0^{-1}$.

ployed. During the simulation, each flagellum has a constant frequency f chosen from a Gaussian distribution with the average $f_0 = 1/120\tau_0^{-1}$ and the variance $\langle (f - f_0)^2 \rangle = \sigma^2 f_0^2$, where σ is a dimensionless number characterizing the width of the frequency distribution. When the average spontaneous curvature c_0 is positive, the flagellum is curved and prefers a clockwise circular trajectory. The trajectory diameter D_0 depends approximately linearly on $(c_0 l_0)^{-1}$ in AF simulations, and the center-of-mass velocity v_{f_0} of the flagellum decreases approximately linearly with $c_0 l_0$ from its value for $c_0 = 0$, as shown in Fig. 2. Each simulation runs for at least $2500/f_0$. The other parameters of our flagellum simulations are listed in Ref. 54.

The collision of two particles with elongated structure in a viscous fluid environment results in a cooperated motion that the particles move together with close packing. If the elongated particles are straight, the nematic interaction results in velocity alignment of neighbor particles and cluster formation in velocity alignment of neighbor particles and cluster formation [10, 11, 25]. When two elongated and curved flagella encounter each other, they tend to get close and synchronize their configuration via hydrodynamic interactions as well as volume exclusion [11, 15] and form an effective “extended flagellum” with the same average curvature. The circular motion of such an extended flagellum around a center is equivalent to the motion of two flagella around the same center, the first step towards the formation of a vortex.

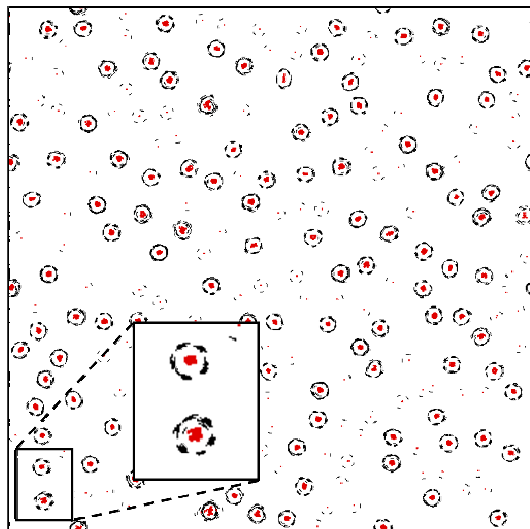


FIG. 3. (Color online) A snapshot of vortices in a circle SPPs system at the end of the simulation time $t = 4 \times 10^3 T_0$. Each black dash is the trajectory of a particle in a time interval $\Delta T = 10\Delta t \approx 0.08T_0$, and the red dots are the corresponding trajectory centers. The inset shows a magnification of the area at the bottom left corner where two vortices consists of groups of circle SPPs with equal distance between neighboring groups. The number of particle groups of them are five and six, respectively. The parameters are $L_x = L_y = 40D_0$, $\rho_0 D_0^2 = 4$, and $d = 1.3D_0$.

III. COLLECTIVE MOTION OF CIRCLE SPPS

N circle SPPs are distributed in the simulation box with random positions and random velocity directions at the initial time $t = 0$. Shortly after the start, vortices emerge, which are formed by one or several particles circling around a common center, as illustrated in Fig. 3 and movies in the supplemental material [55]. The vortices distribute in space with no obvious long-range order, and displace vigorously if the trajectory centers of the particles belonging to the same vortex do not coincide precisely at the same point. When two vortices overlap or collide, particles are exchanged between the vortices until they either fuse or separate from each other far enough. Therefore, the vortex mass, defined as the number of circle SPPs forming it, changes during collisions. Note that the system is deterministic due to the absence of noise, and a noise-induced fission of vortices does not occur in the simulation. We characterize the emergent vortex pattern of circle SPPs by the particle density-correlation functions, the trajectory-center density-correlation functions, and the order parameter reflecting the degree of the particle aggregation. By systematically

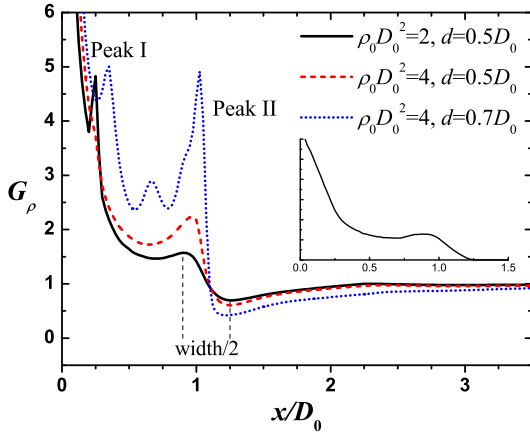


FIG. 4. (Color online) The examples of the particle-density correlation function G_ρ . The inset is the density correlation function of an annular region of evenly distributed particle density. The diameter of the inner circle of the annular region is $0.75D_0$, and the diameter of the outer circle is $1.25D_0$.

changing the particle density ρ_0 and the size of the interaction region d , we then determine the dynamics phase diagram of this system.

A. Particle density-correlation functions and trajectory-center density-correlation functions

The correlation function of particle densities at time t is given by

$$G_\rho(|\mathbf{r} - \mathbf{r}'|) = \rho_0^{-2} \langle \rho(\mathbf{r}, t) \cdot \rho(\mathbf{r}', t) \rangle_t, \quad (3.1)$$

and the correlation function of the trajectory-center density at time t is

$$G_c(|\mathbf{r} - \mathbf{r}'|) = \rho_0^{-2} \langle \rho_c(\mathbf{r}, t) \cdot \rho_c(\mathbf{r}', t) \rangle_t, \quad (3.2)$$

where $\rho(\mathbf{r}, t)$ and $\rho_c(\mathbf{r}, t)$ are the number densities of the particles and the trajectory centers at position \mathbf{r} and time t , respectively. We consider times t in the interval $[T_1, T_2]$, where $T_1 = 8 \times 10^2 T_0$ and $T_2 = 4 \times 10^3 T_0$. Most of the systems have not yet reached a stationary state at $t = T_1$, so that the correlation functions $G_\rho(x, t)$ and $G_c(x, t)$ still contain some averaging over different structures and spatial arrangements of the vortices.

The particle density-correlation function $G_\rho(x)$ mainly characterizes particle arrangement in a vortex, in particular for $x < D_0 + d/2$, as shown in Fig. 4. In the single-vortex region, $G_\rho(x)$ displays a pronounced spatial dependence. There

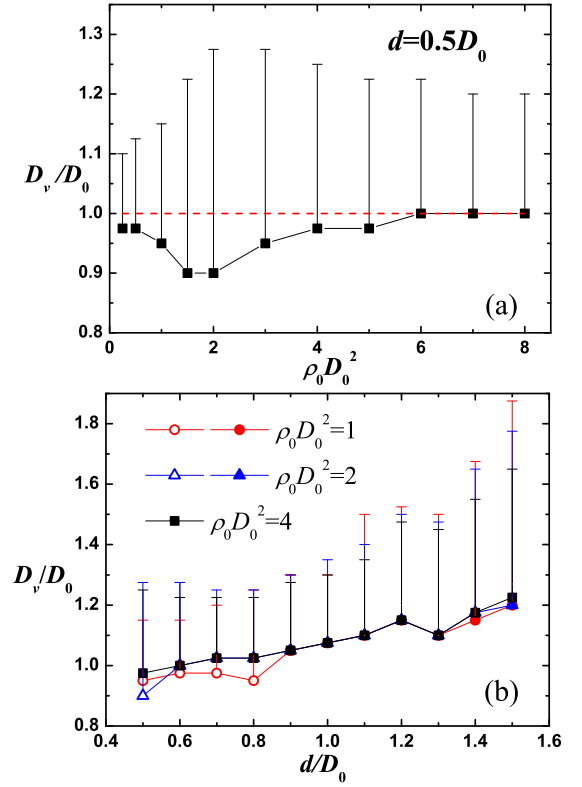


FIG. 5. (Color online) (a) The vortex diameter D_v as a function of the particle density $\rho_0 D_0^2$. The red dashed line is the guide to the eye at value $D_v = D_0$. (b) D_v as a function of the diameter of the interaction region d . The open symbols and the solid symbols represent the light-vortex-dominated systems and the heavy-vortex-dominated systems, respectively. The error bars in (a) and (b) are the half width of peak II as defined in Fig. 4.

is a pronounced peak at $x \approx d/2$, denoted as peak I, which arises from the interaction range of our model. The displacement of a particle in a simulation time step, $v_0 \Delta t$, is much smaller than $d/2$; therefore, during the very short time interval for two particles to adjust their motion and form a vortex, their relative distance remains essentially constant. This distance only changes when a third particle comes into play. If the mass of a vortex is high, the multi-particle interaction affects and disturbs the distances of other particles in a vortex. Thus, a higher density ρ_0 depresses peak I in Fig. 4. For example, when $d = 0.5D_0$, doubling ρ_0 strongly depresses the height of peak I. Similarly, increasing d enhances peak I when ρ_0 is kept constant. Therefore, a vortex is composed of several groups of particles with the constant distance $d/2$ between neighbor groups, as illustrated in Fig. 3. If the tendency to keep the distance $d/2$ is strong for the particle groups, a

second and third peak become evident, see Fig. 4. The position of the n -th peak is approximately $x_n = D_v \sin(n\theta/2)$ where $\theta = 2 \arcsin(d/2D_v)$ and D_v is the diameter of the vortex. Note that such periodic particle density modulation is a dynamic temporary structure which breaks and reconstructs with time.

The peak of the vortex structure at $x \simeq D_0$, denoted as peak II, indicates the diameter D_v of a vortex. According to the definition of the density correlation function G_ρ , this diameter is weighted by the mass of the vortices, so that the vortices consisting of more particles contribute more to D_v . Thus, D_v mainly reflects the diameter of the ‘‘heavy’’ vortices, containing a large number of particles in the vortex. We define the width of peak II as the distance between the peak position and the position of the subsequent minimum. A larger peak width indicates a wider band of particles in the vortex. In the low-density limit, the particles hardly meet each other, and the vortices mainly contain a single SPP, which is defined as a light-vortex-dominated state. In this state, $D_v \approx D_0$ and the width of peak II is narrow, as illustrated in Fig. 5a for $\rho_0 D_0^2 < 1$. At high particle density, e.g. for $\rho_0 D_0^2 \geq 4$, a majority of the particles belongs to vortices of mass larger than 10, which is defined as a heavy-vortex-dominated state. In this state, D_v still approximately equals D_0 , but the width of peak II is about twice as large as for $\rho_0 D_0^2 < 1$. An extraordinarily large width at $\rho_0 D_0^2 = 2$ in Fig. 5a indicates a transition of the system from a light-vortex-dominated state to a heavy-vortices-dominated state.

The same transition from light to heavy vortices also happens with increasing d at constant density ρ_0 . The vortex diameters D_v for different $\rho_0 D_0^2$ coincide in the heavy-vortex-dominated state, but are slightly smaller in the light-vortex-dominated state, see Fig. 5b. Increasing d causes a systematic increase of D_v . The small dip at $d = 1.3D_0$, can be interpreted as follows. D_v is not only determined by the spontaneous trajectory diameter D_0 of circle SPPs, but also influenced by the interaction range d , because the vortex prefers a dynamic temporary state with an integral number of particle groups with a constant neighboring distance $d/2$, as shown in Fig. 3. Therefore, D_v can be estimated by $D_v \approx d/[2 \sin(\pi/n)]$, where n is the number of particle groups in a vortex; this estimate provides qualitatively the correct trend for $d \geq 1.1D_0$, but deviates a little quantitatively because n differs for different vortices in the system. For example, heavy vortices with $n = 5$ are dominant when $\rho_0 D_0^2 = 4$ and $d = 1.5D_0$, while there are

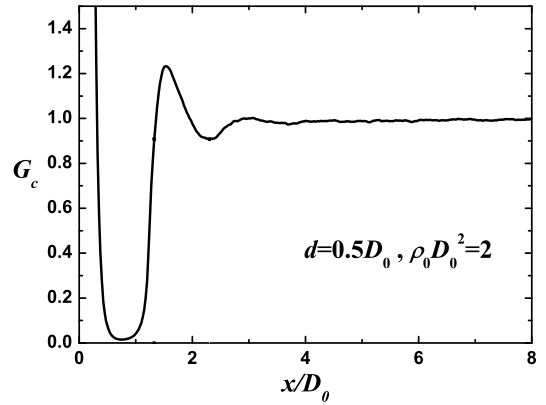


FIG. 6. The trajectory-center-density correlation function, G_c , with $d = 0.5D_0$ and $\rho_0 D_0^2 = 2$.

many heavy vortices of both $n = 5$ and $n = 6$ when $\rho_0 D_0^2 = 4$ and $d = 1.3D_0$.

For $x > D_0 + d$, G_ρ approaches unity due to the loss of spatial correlations at large distances, which indicates a liquid-like order of the vortices.

The correlation function of the trajectory-center density, G_c , shown in Fig. 6, has a large peak at $x = 0$ because of the aggregation of the trajectory centers. G_c decays rapidly to zero for $x \simeq 0.5D_0$, indicating that the trajectory centers aggregate in a small spot at the center of the vortex. Two heavy vortices cannot overlap, otherwise they will fuse into one or separate into several distinct vortices. Therefore, G_c displays a depletion zone from D_0 to $D_0 + d/2$. For $x \geq D_0 + d/2$, G_c increases rapidly and displays a peak corresponding to the the closest possible distance D_{vv} of two neighboring heavy vortices. For larger distances x , G_c approaches a constant with decaying oscillations, which reveals the absence of long-range order and corresponds to a liquid-like spatial arrangement of vortices.

The dependence of D_{vv} on the particle density is show in Fig. 7a. D_{vv} is nearly independent of density, with $D_{vv} \approx 1.55D_0$ for $d = 0.5D_0$ and $\rho_0 D_0^2 \geq 3$, when the system is heavy-vortices dominated. Similarly, $D_{vv} \approx 1.25D_0$ for $\rho_0 D_0^2 \leq 1$, when the system is light-vortices dominated. The transition between light-vortices-dominated and heavy-vortices-dominated states occurs when $1 \leq \rho_0 D_0^2 \leq 3$, which agrees with the transition region extracted from G_ρ (compare Fig. 5a). As shown in Fig. 7b, the increase of D_{vv} with d for constant density $\rho_0 D_0^2$ is somewhat faster than the linear relation $D_0 + d$. For $\rho_0 D_0^2 = 1$, D_{vv} displays a pronounced increase by more than $1.5D_0$ when d is increased from $0.5D_0$ to $1.5D_0$.

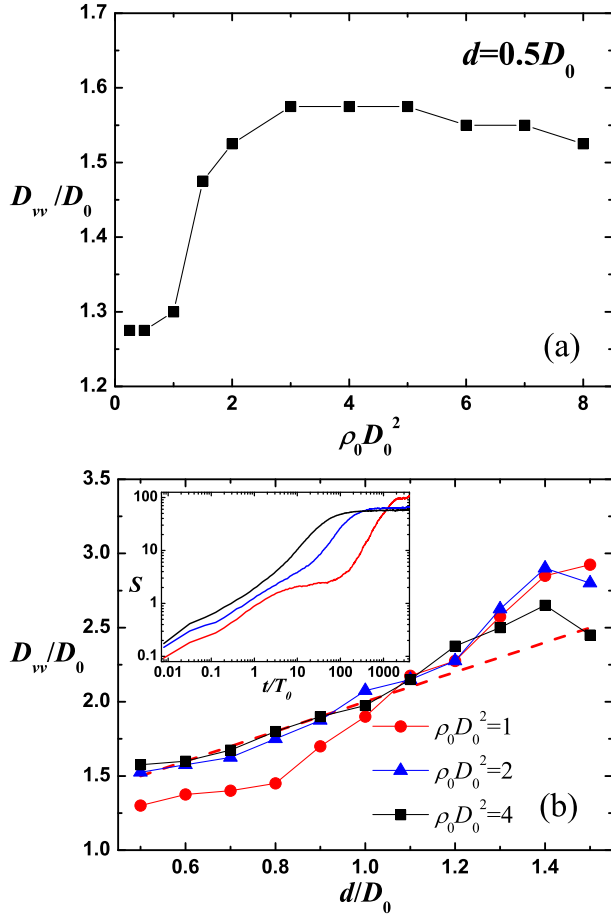


FIG. 7. (Color online)(a) The distance between vortices D_{vv} , as a function of the particle density $\rho_0 D_0^2$. (b) D_{vv} as a function of the diameter of the interaction region d with different particle densities. The red dashed line is $y = D_0 + d$. The inset is the order parameter S as a function of time t/T_0 when $d = 1.5D_0$. The red, blue and black lines represent the particle densities $\rho_0 D_0^2 = 1, 2$, and 4 , respectively.

When $\rho_0 D_0^2 = 2, 4$, D_{vv} exhibits an unexpected decrease for $d = 1.5D_0$; we interpret this as the absence of a second vortex-mass-increasing time period due to the inadequate simulation time, as will be explained in Sec. III B below.

B. Order parameter

In the initial state, all particles are randomly distributed in space, so that the number of the particles and the number of the trajectory centers in a defined area assumes a binomial distribution. When the particles form vortices, the aggregation of the trajectory centers cause a large deviation of the number of trajectory centers in a defined area from its average value. A

stronger aggregation leads to a larger center-density deviation. Therefore, we define an order parameter S as

$$S = \frac{\Delta^2}{\Delta_0^2} - 1, \quad (3.3)$$

where

$$\Delta_0^2 = \frac{ND_0^2}{L_x L_y} \left(1 - D_0^2/L_x L_y\right). \quad (3.4)$$

is the variance of a binomial distribution of point particles, and Δ^2 is the variance of the trajectory center numbers in an area D_0^2 . If the center positions are randomly distributed in the space, S vanishes. S increases with the degree of the aggregation of centers, which indicates the formation of vortices. If all particles circle around a common center, $S = N - 1$.

Suppose N particles form N_v vortices in the two-dimensional space $L_x \times L_y$. The number of the vortices consisting of n particles is $P(n)$, and

$$\sum_n P(n) = N_v, \quad \sum_n nP(n) = N. \quad (3.5)$$

In order to elucidate the relation between the average mass $\langle n \rangle = N/N_v$ of the vortices and the order parameter, we assume that the trajectory centers of all particles in a vortex collapse into one point, the vortex center, although they always have some narrow distribution around the center in the simulations. According to the trajectory-center density correlation function G_c (Fig. 6a), the distance between two vortices in our systems is usually larger than $1.5D_0$ in the systems dominated by heavy vortices, except when two vortices are colliding and merging. Therefore, the possibility to find two heavy vortex center in an area D_0^2 is low. Thus, we assume that the probability to find two vortex centers in D_0^2 is zero. We divide our system of size $L_x \times L_y$ into boxes of size D_0^2 , and fill the boxes with at most one vortex. Then, the variance of the center-number distribution in D_0^2 is

$$\Delta^2 = \frac{D_0^2}{L_x L_y} \left(\sum_n n^2 P(n) - \rho_0 D_0^2 N \right). \quad (3.6)$$

Note that the weight average of the vortex mass is

$$\bar{w} = \sum_n n^2 P(n) / \sum_n n P(n). \quad (3.7)$$

Thus, Δ^2 can be written in terms of \bar{w} as

$$\Delta^2 = \frac{ND_0^2}{L_x L_y} (\bar{w} - \rho_0 D_0^2). \quad (3.8)$$

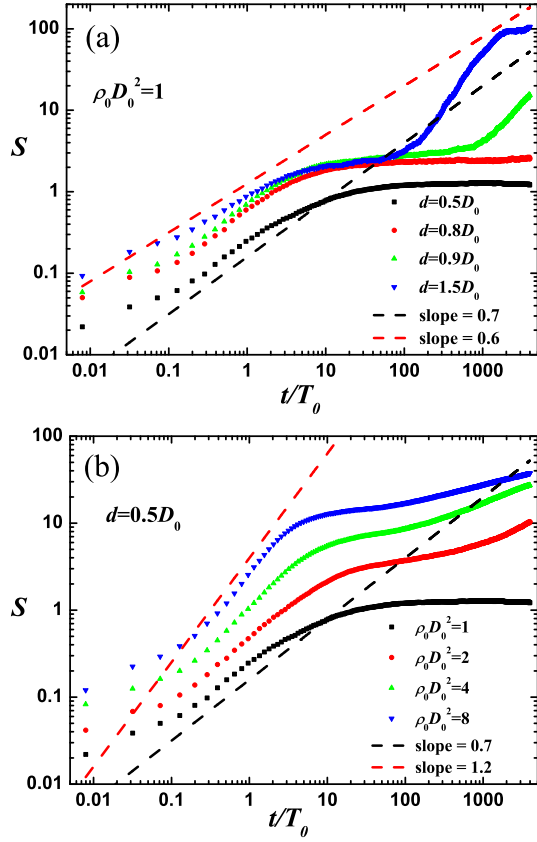


FIG. 8. (Color online) Time evolution of the order parameter S , for (a) various diameters d of the interaction region, and (b) various particle densities ρ_0 . The dashed lines are power laws with different exponents, as indicated.

Substituting Eqs. (3.4) and (3.8) into Eq. (3.3), we find

$$S = \frac{\bar{w} - \rho_0 D_0^2}{1 - D_0^2/L_x L_y} - 1. \quad (3.9)$$

In our simulations, $D_0^2/L_x L_y \leq 1/400 \ll 1$ is negligible, so that

$$S \approx \bar{w} - \rho_0 D_0^2 - 1. \quad (3.10)$$

This result reveals a simple linear relation between our order parameter S and the weight average of vortex mass. Thus, S is a proper order parameter to characterize the degree of vortex formation.

The order parameter S increases with time once the particle start to move and the trajectory centers aggregate, as shown in Fig. 8. S first undergoes a fast increase during a time interval which we call period I. The increase of S with time during period I occurs faster for larger ρ_0 , but is not sensitive to d , as indicated by the dashed lines in Fig. 8. During

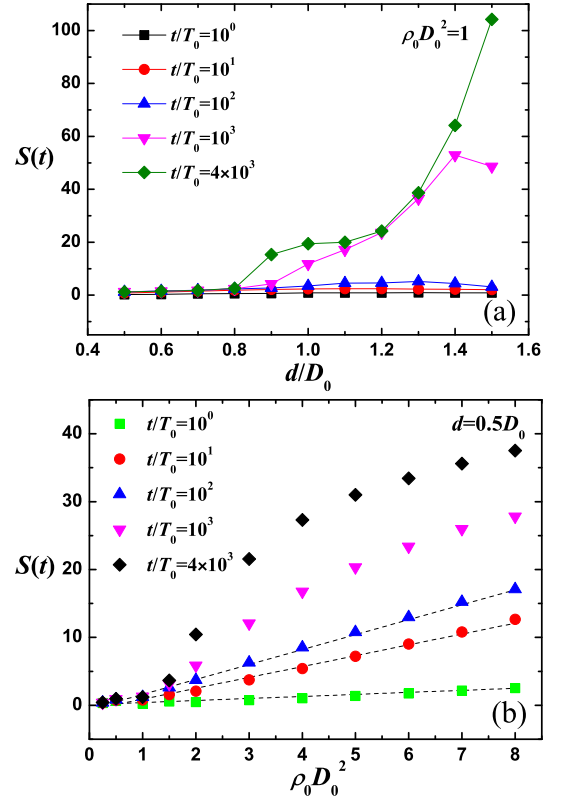


FIG. 9. (Color online) Order parameter S at times $t/T_0 = 10^0, 10^1, 10^2, 10^3$, and 4×10^3 , (a) as a function of d when $\rho_0 D_0^2 = 1.0$, and (b) as a function of $\rho_0 D_0^2$ when $d = 0.5D_0$. The dashed lines in (b) are linear fits of S at $t/T_0 = 10^0, 10^1$, and 10^2 .

this period, the vortices are formed mainly by particles which are close to each other in the initial state; therefore, S depends roughly linearly on the particle density, as shown in Fig. 9b. Period II is defined as the time period after period I, during which S increases only very slowly and approaches a plateau, as shown in Fig. 8. The plateau has a higher value for larger ρ_0 and d .

For high densities ($\rho_0 D_0^2 \geq 2$ when $d = 0.5D_0$ in Fig. 8b) or large d ($d \geq 0.9D_0$ when $\rho_0 D_0^2 = 1$ in Fig. 8a), there is another dynamical evolution after period II, denoted period III, in which S displays another pronounced increase. The increase of S in period III indicates the formation of heavy vortices by vortex fusion — not seen for some low ρ or small d systems. However, in our simulation time scale, some systems with high ρ and large d also do not display period III (see the inset of Fig. 7b), in this case because the simulation time is not long enough for vortex fusion to occur.

By analyzing the order parameter S at a given time t for different systems, we can also determine the transition

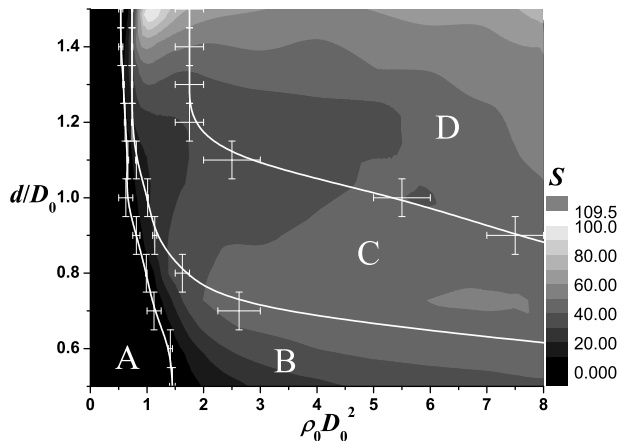


FIG. 10. Phase diagram of the circle SPPs system. The color from black to white shows the value of S at $t/T_0 = 4 \times 10^3$ from 0 to 10^2 . The white lines divide the phase diagram into four regimes according to the shape of $S(t)$. For the definition of regimes A to D see main text.

from the light-vortex-dominated state to the heavy-vortex-dominated state, as shown in Fig. 9. The transition happens when $0.8 \leq d/D_0 \leq 1.0$, for $\rho_0 D_0^2 = 1$, and when $1 \leq \rho_0 D_0^2 \leq 3$ for $d = 0.5D_0$. S assumes a small value near zero in the light-vortex-dominated systems, then increases rapidly with increasing d and $\rho_0 D_0^2$ in the heavy-vortex-dominated systems.

According to the different shapes of $S(t)$ for different systems, compare Fig. 9, we obtain the phase diagram of circle SPPs, as shown in Fig. 10. The phase diagram is divided into four regimes. For systems locating in regime A, S has completed the first growth period I, and reached the plateau of period II, i.e. the final state of these systems (at $t/T_0 = 4 \times 10^3$) is dominated by light vortices. In regime B, the systems have passed the stationary period II, and at the end of the simulation time are just undergoing the fusion of light vortices (period III); thus, these systems are in the crossover between regimes A and C. In regime C, the systems have come to the second stationary state after the pronounced increase of S in period III. Finally, in regime D, which occupies the high ρ and high d section of the phase diagram, the evolution of the fusion of heavy vortices is still in progress at $t/T_0 = 4 \times 10^3$; the end state is characterized in this case by heavy vortices of similar weight.

Note that the division of the regimes according to the temporal evolution of $S(t)$ resembles but does not coincide with a classification according to the value of S in the final

state state. For example, S does not have the highest value in regime D. The reason is that the characteristic time scale of the evolution strongly depends on particle density, so that at the chosen final simulation time, the systems in regime D has only been able to complete the initial collection of neighbor particles. (see inset of Fig. 7b).

Our simulations are performed without noise. Therefore, the vortex mobility only depends on multi-particle interactions. Increasing vortex mass leads to an increasing complexity of these interactions and can result in a high mobility of vortices. The light-vortex-dominated systems cannot increase the vortex mass via collision because all vortices do not move after formation. In contrast, systems which form heavier vortices during period I can continue to increase the vortex mass via the collision of vigorous heavy vortices until a limit is reached, which is determined by the particle density. At the boundary between regimes A and B in Fig. 10, the value of S is between 1 and 3, indicating the weighted vortex mass less than 5. Moreover, the position of the line agrees well with the transition between light-vortex-dominated state and heavy-vortex-dominated state indicated by the variation of D_v and D_{vv} shown in Fig. 5 and Fig. 7. Therefore, the boundary between regimes A and B can be identified with the transition from the light-vortex-dominated to the heavy-vortex-dominated state.

IV. COLLECTIVE MOTION OF CURVED, SINUSOIDALLY-BEATING FLAGELLA

The flagella are initially distributed randomly in space, with random orientations. Shortly after the flagella start beating, the system reaches a stationary state in which the curved flagella spontaneously organize into rotating vortices [55], as illustrated in Fig. 11ab. The flagella are moving clockwise and the waves on the flagella are propagating counter-clockwise. In AF simulations, the flagella only have hard-core interactions, while in a MPC fluid, the hydrodynamic interactions synchronize the flagellar beat in the same vortex and packs flagella tightly due to hydrodynamic attraction [15]. The mass of each vortex changes dynamically due to the collision with flagella in neighboring vortices [55].

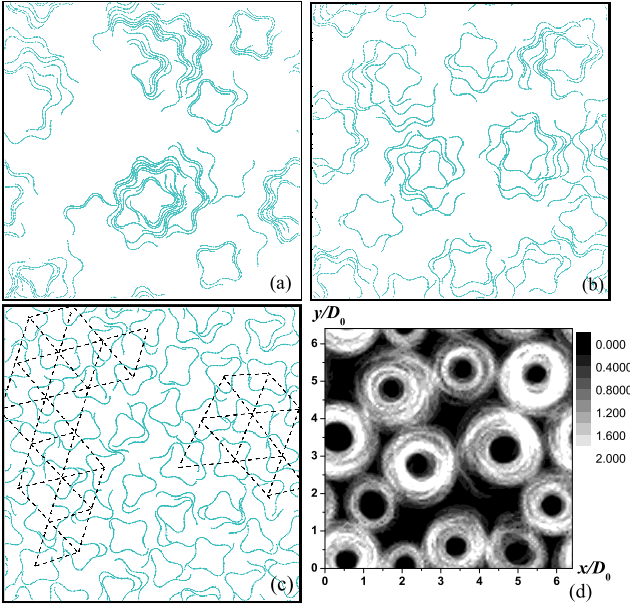


FIG. 11. (Color online) Snapshots of self-organized vortices of flagella (a) in a MPC fluid with $D_0 = 30.7a$, $\rho_0 D_0^2 = 2.36$, and $\sigma = 0\%$, (b) in AF with $D_0 = 30.7a$, $\rho_0 D_0^2 = 2.36$, and $\sigma = 0\%$, and (c) in AF with $D_0 = 16.4a$, $\rho_0 D_0^2 = 0.67$, and $\sigma = 0\%$. The dashed lines in (c) shows the local hexagonal order. (d) Normalized flagellum density $\bar{\rho}_f(\mathbf{r})$ averaged over a time interval of $\Delta T = 30/f_0$ of the system in (b). See also movie S1 in the supplemental material [55].

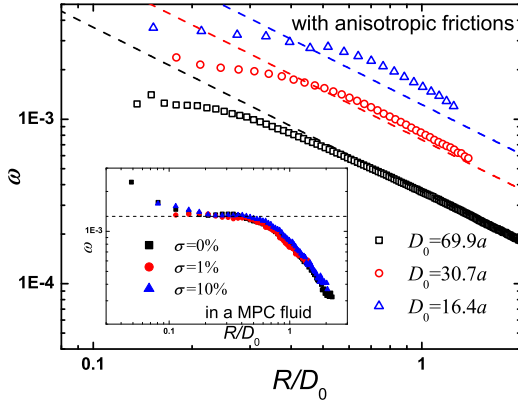


FIG. 12. (Color online) Angular velocity ω of the vortex as a function of the radius position in AF simulations with $\rho_0 = 0.0025a^{-2}$ and $\sigma = 0\%$. The dashed lines are the functions $\omega = v_{f,0}R^{-1}$. The inset shows ω as a function of R in a MPC fluid with $\rho_0 D_0^2 = 2.36$ and $D_0 = 30.7a$; the dashed line is a guide to the eye to indicate a plateau.

A. Angular swimming velocities

Figure 12 shows the angular velocity $\omega = v_f/R$, where v_f is the center-of-mass velocity of a flagellum and R is the distance between the mass center of the flagellum and the

vortex center to which the flagellum belongs, as a function of R . In AF simulations, ω approaches $v_{f,0}/R$ for large R , where $v_{f,0}$ is the velocity of a freely swimming flagellum. At small radii, the volume exclusion between the propagating sinusoidal configurations of neighboring flagella reduces the angular velocity. Thus, although ω still slowly increases with decreasing R for $R < 0.5D_0$, it is much lower than expected from the relation $\omega = v_{f,0}/R$. On the other hand, at large radius ($R > 0.5D_0$), in some AF systems (for example, $D_0 = 30.7a$ and $D_0 = 16.4a$ in Fig. 12), ω is larger than $v_{f,0}/R$ due to the repulsive interaction between two flagella belonging to different vortices. In conclusion, the volume exclusion between the flagella depresses ω due to interactions between flagella in the same vortex, but enhances ω due to interactions between neighboring vortices.

In a MPC fluid, ω also approximately obeys the power law $\omega \sim R^{-1}$ at large R . However, at radii $0.2 < R/D_0 < 0.5$, ω is nearly independent of R , as shown in Fig. 12b. Here, the synchronized flagella form a closed ring with integer numbers of waves and rotate with same angular velocity, as shown in movie S2 in the supplementary material [55].

Although ωR is not exactly equal to $v_{f,0}$ in systems with MPC fluid or with AF, an assumption of a unique swimming velocity is still a good approximation for comparison of the flagella system with the circle SPPs system.

B. Correlation functions

We define a normalized density of flagellar segments as

$$\bar{\rho}_f(\mathbf{r}, t) = \frac{1}{\Delta T} \int_{t-\Delta T/2}^{t+\Delta T/2} dt \frac{\rho_f(\mathbf{r}, t)}{\rho_{f,0}}, \quad (4.1)$$

where $\rho_f(\mathbf{r}, t)$ is the number density of monomer beads averaged in a square box of area $(L_x/100) \times (L_y/100)$ at the position \mathbf{r} at time t . In order to gain better statistics of the vortex structures, $\bar{\rho}_f$ is the average over time ΔT , with ΔT is chosen to be $30/f_0$. An example of an image of $\bar{\rho}_f(\mathbf{r}, t)$ is shown in Fig. 11d.

The correlation function of flagellum density is then defined as

$$G_{f,\rho}(|\mathbf{r} - \mathbf{r}'|) = \langle \bar{\rho}_f(\mathbf{r}, t) \cdot \bar{\rho}_f(\mathbf{r}', t) \rangle_t. \quad (4.2)$$

Similarly, the correlation function of flagellum trajectory-center density is

$$G_{f,c}(|\mathbf{r} - \mathbf{r}'|) = \langle \bar{\rho}_{f,c}(\mathbf{r}, t) \cdot \bar{\rho}_{f,c}(\mathbf{r}', t) \rangle_t. \quad (4.3)$$

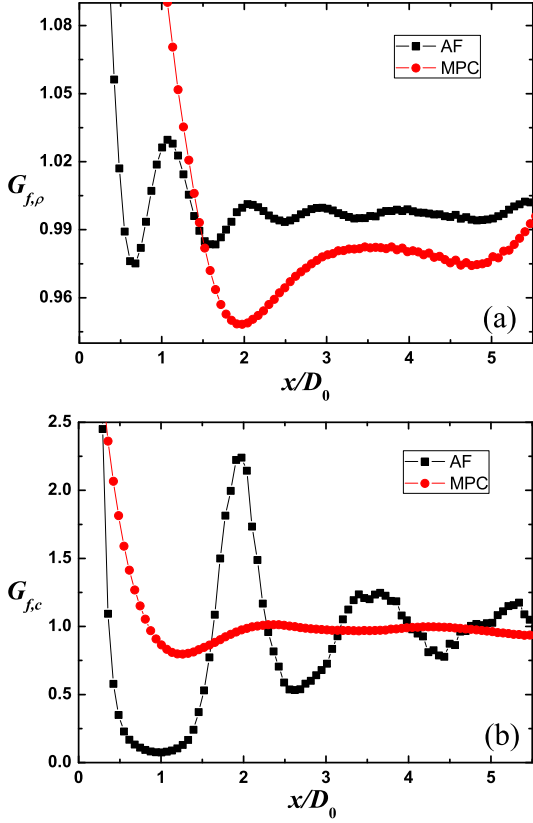


FIG. 13. (Color online) Correlation functions of (a) the normalized flagellum density $\bar{\rho}_f(\mathbf{r})$ and (b) the normalized trajectory center density $\bar{\rho}_{f,c}(\mathbf{r})$. Both densities $\bar{\rho}_f(\mathbf{r})$ and $\bar{\rho}_{f,c}(\mathbf{r})$ are averaged over a time interval $\Delta T = 30/f_0$. The parameters are $D_0 = 30.7a$, $\rho_0 D_0^2 = 2.36$, and $\sigma = 0\%$. The symbols indicate the results of MPC-fluid (red bullets) and of AF (black squares) simulations.

where $\bar{\rho}_{f,c}(\mathbf{r}, t) = \rho_{f,c}(\mathbf{r}, t)/\rho_{f,0}$ and $\rho_{f,c}(\mathbf{r})$ is the number density of the centers of flagellum trajectories at \mathbf{r} and time t . Figures 13a,b show examples of $G_{f,\rho}$ and $G_{f,c}$, respectively. Both correlation functions approach a constant at large distances, indicating the absence of long-range order and a liquid-like arrangement of vortices, similarly as discussed for circle SPPs in Sec. III A. Long-range order of vortices, such as a hexagonal arrangement, is not observed even for large flagellum densities. However, a local hexagonal order is still possible due to the volume exclusion between vortices, as indicated by the higher-order peaks of $G(r)$ and shown in real-space snapshots in Fig. 11c.

The interpretation of the correlation function is of course very similar as for correlations functions of circle SPPs in Sec. III A. The first local maximum of $G_{f,\rho}$ corresponds to the average vortex diameter, the first local maximum of $G_{f,c}$

to the average distance between neighbor vortices. A comparison of AF and MPC simulations clearly shows that structures in the vortices in the AF model are considerably more ordered, which leads to pronounced oscillations of the correlations functions. In the AF simulations, $G_{f,c}$ nearly vanishes at $x \simeq D_0$, indicating that the area occupied by the trajectory centers in a vortex is significantly smaller than D_0 , in agreement with our circle SPPs observations. In the MPC-fluid simulations, the weaker correlations indicate a larger diversity of vortex sizes but also a larger mobility of the vortices.

A comparison of the snapshots and correlation functions in Figs. 11 and 13b with those of sea-urchin sperm vortices in Ref. 31 shows that the phenomena observed in AF simulations are more similar to the experimental behavior than those in MPC simulations. Furthermore, the results of our AF simulations agree much better with those of our circle SPPs simulations. We attribute the deviations of the MPC-simulation results from those of the experiments to the very strong hydrodynamic interactions in the two-dimensional model system. Indeed, the flow field around a dragged point particle in two spatial dimensions decays only logarithmically with distance r , while in three dimensions it decays much faster, like $1/r$, and even faster in the presence of a wall. In the experiments, the motion of sperm near a wall is governed by three-dimensional hydrodynamics. Thus, we conclude that a detailed numerical investigation of the importance of hydrodynamic interactions for the formation of sperm vortices requires full three-dimensional hydrodynamic simulations. The two-dimensional MPC simulation still provide the important information that the synchronized flagellum beating of the sea-urchin sperms in a vortex is the result of hydrodynamic interactions between the beating tails, as indicated by the snapshot in Fig. 11a (see also Refs. 11 and 15). In the remainder of this section, we focus on the analysis of the systems with anisotropic friction.

C. Vortices of flagella in the anisotropic-friction model

Figure 14 shows the average vortex diameter D_v and the average vortex distance D_{vv} as functions of ρ_0 , D_0 , and σ . In the low-density limit, the flagella move without touching each other. Thus D_v must approach D_0 and D_{vv} must approach the average distance between flagella. As the density increases, D_v and D_{vv} increase slowly, as shown in Fig. 14a. As in the

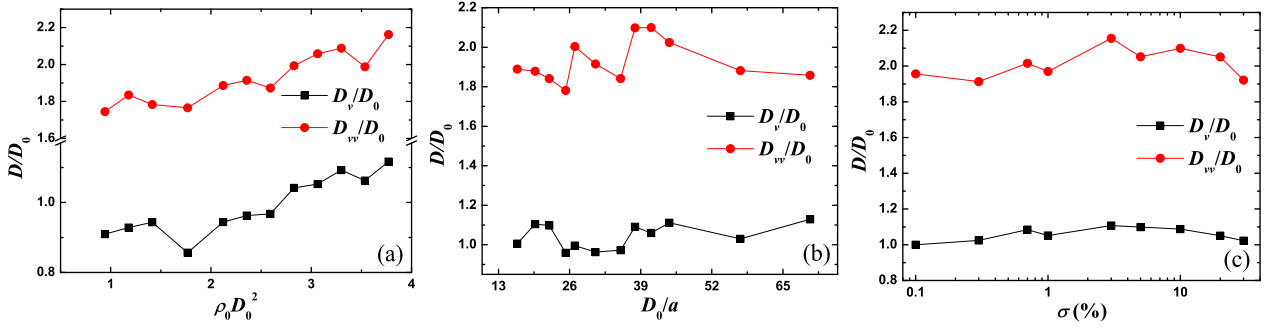


FIG. 14. (Color online) Vortex diameter D_v and average distance between vortices D_{vv} as a function of (a) the flagellum density ρ_0 , (b) the spontaneous trajectory diameter D_0 , and (c) the variance σ of frequency distribution in AF simulations.

circle SPPs systems, compare Figs. 4 and 7, D_v and D_{vv} also increase and level off when $2 \leq \rho_0 D_0^2 \leq 4$. However, the drop of D_v and D_{vv} near $\rho_0 D_0^2 = 2$ for circle SPPs systems, which indicates the transition from the light-vortex-dominated to the heavy-vortex-dominated state, is not seen in the curved-flagella system. On the other hand, the increase of D_v can also partially be attributed to the volume exclusion between flagella, so that the orbit at radius R in the vortex can be occupied only by a limited number of flagella. Similarly, D_{vv} increases with $\rho_0 D_0^2$ due to volume exclusion, which generates an effective repulsion between the neighboring vortices.

When we change the preferred trajectory diameter D_0 of the curved flagella, the diameter of a vortex varies as $D_v \approx D_0$, as shown in Fig. 14b, in good agreement with the behavior of the circle SPPs systems. However, over a wide range of ρ_0 or D_0 , D_{vv}/D_0 remains nearly independent of these parameters and fluctuates around a value 1.9 ± 0.2 . This value of D_{vv}/D_0 is found for the interaction range $d/D_0 = 0.9$ to 1.0 in circle SPPs systems (Fig. 7b). Thus, we conclude that the effective size of the interaction region of a curved flagellum is approximately the same as the diameter of its circular trajectory.

In the sea-urchin sperm vortex experiment [31], the radius of the sperm vortex is $D_v/2 = 13.2 \pm 2.8 \mu\text{m}$, and the average vortex distance is $D_{vv} = 49 \pm 9 \mu\text{m}$. Therefore, $D_{vv}/D_v = 1.86 \pm 0.52$ in the experiment, in excellent agreement with $D_{vv}/D_v = 1.8 \pm 0.2$ in our AF simulations. In our circle SPPs simulations, $D_{vv}/D_v = 1.83 \pm 0.10$ for systems with $d = 0.9D_0$ in the heavy-vortex-dominated state.

The vortex formation is not sensitive to the width of the beating-frequency distribution of the flagella, as shown in Fig. 14c, although it leads to a range of flagellar velocities. This insensitivity explains the emergence of the vortices in the sea-

urchin sperm experiment even though there is a spread of beating frequency of about 9 percent [31].

Figure 15 shows that the order parameter S , which represents the degree of aggregation and is closely related to the weight average of vortex mass, grows with increasing ρ_0 and D_0 . Interestingly, in the stationary state of the flagella system, S increases linearly with flagellum density when $\rho_0 D_0^2 \leq 3$, which is reminiscent of the linear relation between S and $\rho_0 D_0^2$ for $t/T_0 \leq 100$ in circle SPPs systems (Fig. 9b). However, in circle SPPs systems, S continues to increase after $t/T_0 = 100$. We attribute the linear relation of S and ρ_0 in the flagella system to the effect of volume exclusion. The linear dependence of S on the flagellum density agrees very well with the experimental observations for sea-urchin sperm. On the other hand, S is found to increase as $S \sim D_0^3$, see Fig. 15b, indicating the importance of a second length scale, which should be related to the flagellum length.

D. Discussion

The effect of volume exclusion and synchronization of the flagellar beat manifests itself in the following three main aspects.

First, as shown in Fig. 11bc, the flagellum vortices are closed rings composed of synchronized flagella. This closed structure makes the fusion of large vortices to happen very infrequently, because the necessary force to open such a structure to fuse two neighboring vortices is very large. Therefore, as suggested by our circle SPPs simulations, the flagellum system experiences vortex formation and reorganization only during the early stages of structure formation, corresponding to period I in the circle SPP system, which leads to vortices

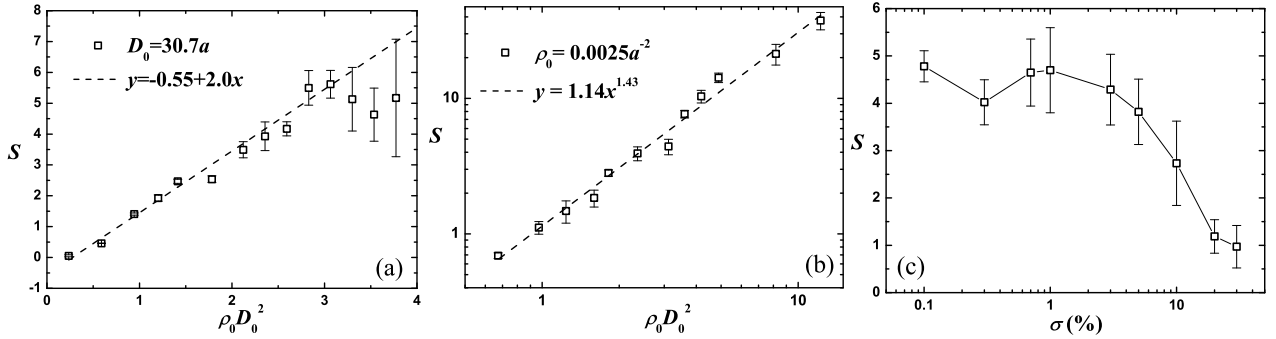


FIG. 15. Order parameter S as a function of (a) the scaled density $\rho_0 D_0^2$, with $D_0 = 30.7a$ and $\sigma = 0\%$, (b) the scaled circle area ρD_0^2 , with $\rho_0 = 0.0025a^{-2}$ and $\sigma = 0\%$, and (c) the width σ of the frequency distribution, with $\rho_0 D_0^2 = 2.36$.

described by an order parameter S which depends linearly on the particle density. The next step to raise the aggregation number, corresponding to period III in the circle SPP system, which requires the fusion of heavy vortices, is prevented by their nearly impenetrable closed structure.

Second, an extraordinary heavy vortex cannot exist for long, because the maximum mass of a vortex is determined by the balance of forces between flagella. For a flagellum swimming at a distance R from the center, the prevalent trajectory curvature is $1/R$, while the preferred trajectory curvature of a flagellum is $2/D_0$. When $R < D_0/2$, the flagellum at R pushes outwards and exert an outward force on other flagella in outer layers; similarly, when $R > D_0/2$, a flagellum at R pushes inwards and exerts an inward force on other flagella in inner layers. When R exceeds D_0 , an instability should develop, which leads to a breakup into smaller vortices of radius $D_0/2$. For systems with larger D_0 , the region $R < D_0/2$ is larger and the typical difference between $1/R$ and $2/D_0$ is smaller, so that the maximum vortex mass is larger than for systems with smaller D_0 . Therefore, S increases with increasing D_0 for fixed ρ_0 , as shown in Fig. 15ab.

Third, consider now a large flagellum density, for which the system is already full of vortices of similar mass, frequently colliding with each other (see movie S3 in supplemental material [55]). A further increase of ρ_0 starts to destroy the vortex structure and the order parameter S decreases, as shown in Fig. 15a for $\rho_0 D_0^2 > 3$. Such a decrease of S was not observed in the sea-urchin sperm experiment [31] because the experimental system was not strictly two-dimensional. We conjecture that at a certain surface density of sperm, the substrate is completely packed with vortices and cannot absorb any more cells. The local hexagonal order of the sperm vortex

array [31] is a clue for this close packing. A further increase of the surface density of sperm is not possible because higher density will cause more frequent collision and consequently expel some sperm from the near-substrate layer. It seems not possible [56] to obtain a higher surface density of sperm than $6000/\text{mm}^2$, the largest density investigated in Ref. 31. For higher densities in the experiments, multiple layers of sperm developed, and the layers on top were neither ordered nor destroying the pattern below [56]. A possibility to increase the density further in experiments might be to restrict the sperm in a narrow slit of one layer thickness between two flat substrates.

The variance σ of the frequency distribution also influence the order parameter, as shown in Fig. 15b. S is not sensitive to σ when $\sigma \leq 5\%$, but decreases with increasing σ for $\sigma > 5\%$. When there are large differences between the frequencies of flagella in a vortex, the collisions between the undulating shapes increase the short-range repulsion, separate the flagella and cause a looser vortex structure, so that vortex break up more easily in collisions with other vortices. At small $\sigma < 5\%$, this effect is small. Note that even for $\sigma = 30\%$, vortices still exist, as indicated by the density correlation functions. However, stable structures hardly exist for a long time. The frequent fission and fusion of vortices make S small, although the system is not completely disordered.

V. SUMMARY & CONCLUSIONS

We have simulated systems of self-propelled particles with preferred circular trajectories (circle SPPs) interacting via a velocity-trajectory coordination rule, and systems of curved flagella propelled by a sinusoidal beating motion. In

both systems, we observe the formation of vortex arrays, controlled by particle density, interaction range, and diameter of the preferred circular trajectory.

For the circle-SPP systems, the vortex array shows liquid-like rather than hexagonal spatial order. The diameter of the vortices, D_v , is about the diameter of a single particle trajectory D_0 with a slight increase with the diameter of the interaction region d , but is not sensitive to the particle density ρ_0 . The average distance between neighbor vortices, D_{vv} , is also not sensitive to ρ_0 , but increases quickly with increasing d . A transition from a light-vortex-dominated state (at low ρ_0 and small d) to a heavy-vortex-dominated state (at high ρ_0 or large d) is observed.

We use an order parameter S to characterize the degree of the vortex formation. By comparing the time evolution of S , we find that the vortex formation can be divided into three time periods. During period I, the particles collect neighbor ones to form vortices and S increase quickly with time. The increase of $S(t)$ during period I is slightly elevated with ρ_0 , but is not sensitive to d . In the subsequent period II, $S(t)$ increases very slowly. In period III, the vortex mass increases again more rapidly through vortex collision and fusion. Note that environmental noise is not described in our model. Therefore the fission, fusion and displacement of vortices is purely the result of multi-particle interactions of circle SPPs.

In order to compare with the experiments of sperm cells near surfaces, we have also studied a more detailed model of curved, sinusoidally beating flagella. Vortex patterns in this system emerge from the hard-core repulsion of the curved body of the elongated self-propelled particles moving in a viscous environment. In the simulations with anisotropic frictions, the collective motion of the curved flagella system agrees very well with the behavior of the circle SPPs system,

as well as the phenomenon observed in the sea-urchin sperm experiments [31]. As in the circle SPPs system, the average size of the vortices D_v equals approximately D_0 , and slightly increases with the flagellum density. By comparing D_{vv} with the circle SPPs systems, we find that the size of the effective interaction region of a curved flagellum can be approximately identified with $0.9 \sim 1.0D_0$. The order parameter S increases with ρ_0 as well as D_0 . The fraction $D_{vv}/D_v = 1.8 \pm 0.2$ coincides the value 1.86 ± 0.52 calculated by using the data from [31] for sea-urchin sperm system.

In conclusion, the collective motion of self-propelled particles, which leads to the formation of vortex arrays, can be well reproduced by circle SPPs with a velocity-trajectory coupling interaction. The velocity-trajectory coordination rule is a different interaction type than the velocity coordination rules employed since the Vicsek model [20] for the simulations of collective motion. Such an interaction mimics, for example, the hard-core interaction of curved, sinusoidal beating flagella. The analysis of a more specific model of beating flagella allows to elucidate the features related to an explicit propulsion mechanism and physical interactions.

VI. ACKNOWLEDGMENTS

Y.Y. gratefully acknowledges support from the National Natural Science Foundation of China (Grants 21304020) and the Shanghai Postdoctoral Scientific Program (Program No.11R21411200). G.G. gratefully acknowledges support from the VW Foundation (VolkswagenStiftung) through the program *Computer Simulation of Molecular and Cellular Bio-Systems as well as Complex Soft Matter*.

-
- [1] T. Vicsek and A. Zafeiris, *Phys. Rep.* **512**, 71 (2012).
 - [2] V. Schaller, C. Weber, C. Semmrich, E. Frey, and A. R. Bausch, *Nature* **467**, 73 (2010).
 - [3] T. Butt, T. Mufti, A. Humayun, P. B. Rosenthal, S. Khan, S. Khan, and J. E. Molloy, *J. Biol. Chem.* **285**, 4964 (2010).
 - [4] W. F. Paxton, K. C. Kistler, C. C. Olmeda, A. Sen, S. K. St. Angelo, Y. Cao, T. E. Mallouk, P. E. Lammert, and V. H. Crespi, *J. Am Chem. Soc.* **126**, 13424 (2004).
 - [5] P. Dhar, Th. M. Fischer, Y. Wang, W. F. Mallouk, W. F. Paxton, and A. Sen, *Nano Lett.* **6**, 66 (2006).
 - [6] I. L. Bajec and F. H. Heppner, *Animal Behaviour* **78**, 777 (2009)
 - [7] Y. Hayakawa, *EPL* **89**, 48004 (2010).
 - [8] J. J. Faria, J. R. G. Dyer, C. R. Tosh, and J. Krause, *Animal Behaviour* **79**, 895 (2010).
 - [9] M. Moussaïd, D. Helbing, and G. Theraulaz, *Proc. Natl. Acad. Sci.* **108**, 6884 (2011).
 - [10] F. Peruani, A. Deutsch, and M. Bär, *Phys. Rev. E* **74**, 030904 (2006).
 - [11] Y. Yang, V. Marceau, and G. Gompper, *Phys. Rev. E* **82**, 031904 (2010).

- [12] A. Czirók, E. Ben-Jacob, I. Cohen, and T. Vicsek, *Phys. Rev. E* **54**, 1791 (1996).
- [13] J. P. Hernandez-Ortiz, C. G. Stoltz, and M. D. Graham, *Phys. Rev. Lett.* **95**, 204501 (2005).
- [14] C. M. Pooley, G. P. Alexander, and J. M. Yeomans, *Phys. Rev. Lett.* **99**, 228103 (2007).
- [15] Y. Yang, J. Elgeti, and G. Gompper, *Phys. Rev. E* **78**, 061903 (2008).
- [16] D. Strömbom, *J. Theor. Biol.* **283**, 145 (2011).
- [17] R. A. Simha and S. Ramaswamy, *Phys. Rev. Lett.* **89**, 058101 (2002).
- [18] V. Narayan, S. Ramaswamy, and N. Menon, *Science* **317**, 105 (2007).
- [19] I. S. Aranson, A. Snezhko, J. S. Olafsen, and J. S. Urbach, *Science* **320**, 612 (2008).
- [20] T. Vicsek, A. Czirók, E. Ben-Jacob, I. Cohen, and O. Shochet, *Phys. Rev. Lett.* **75**, 1226 (1995).
- [21] G. Baglietto and E. V. Albano, *Phys. Rev. E* **80**, 050103 (2009).
- [22] V. L. Kulinskii and A. A. Chepizhko, *Math. Stat. Phys.* **1198**, 25 (2009).
- [23] H. Chaté, F. Ginelli, G. Grégoire, F. Peruani, and F. Raynaud, *Eur. Phys. J. B* **64**, 451 (2008).
- [24] L. ZhiXin and G. Lei, *Science China Series F: Information Sciences* **51**, 848 (2008).
- [25] F. Ginelli and H. Chaté, *Phys. Rev. Lett.* **105**, 168103 (2010); F. Ginelli, F. Peruani, M. Bär and H. Chaté, *Phys. Rev. Lett.* **104**, 184502 (2010).
- [26] G. Baglietto and E. V. Albano, *Comp. Phys. Comm.* **180**, 527 (2009).
- [27] T. Ihle, *Phys. Rev. E* **83**, 030901 (2011).
- [28] S. Mishra, A. Baskaran, and M. C. Marchetti, *Phys. Rev. E* **81**, 061916 (2010).
- [29] D. L. Blair, T. Neicu, and U. A. Kudro, *Phys. Rev. E* **67**, 031303 (2003).
- [30] A. Ordermann, G. Balazsi, and F. Moss, *Physica A* **325**, 260 (2003).
- [31] I. H. Riedel, K. Kruse, and J. Howard, *Science* **309**, 300 (2005).
- [32] D. Grossman, I. S. Aranson, and E. Ben Jacob, *New J. Phys.* **10**, 023036 (2008).
- [33] A. Kudrolli, G. Lumay, D. Volfson, and L. S. Tsimring, *Phys. Rev. Lett.* **100**, 058001 (2008).
- [34] U. Erdmann, W. Ebeling, and A. S. Mikhailov, *Phys. Rev. E* **71**, 051904 (2005).
- [35] S. van Teeffelen and H. Löwen, *Phys. Rev. E* **78**, 020101 (2008).
- [36] S. van Teeffelen, U. Zimmermann, and H. Löwen, *Soft Matter* **5**, 4510 (2009).
- [37] R. Ledesma-Aguilar, H. Löwen, and J. M. Yeomans, *Eur. Phys. J. E* **35**, 70 (2012).
- [38] F. Kümmel, B. ten Hagen, R. Wittkowski, I. Buttinoni, R. Eichhorn, G. Volpe, H. Löwen, and C. Bechinger, *Phys. Rev. Lett.* **110**, 198302 (2013).
- [39] R. Dreyfus, J. Baudry, and H. A. Stone, *Eur. Phys. J. B* **47**, 161 (2005).
- [40] E. Lauga, W. R. DiLuzio, G. M. Whitesides, and H. A. Stone, *Biophys. J.* (90), 400 (2006).
- [41] H. D. M. Moore and D. A. Taggart, *Biol. Reproduction* **52**, 947 (1995).
- [42] J. Elgeti, U. B. Kaupp, and G. Gompper, *Biophys. J.* **99**, 1018 (2010).
- [43] J. Gray and H. W. Lissmann, *J. Exp. Biol.* **41**, 135 (1964).
- [44] J. Gray and G. J. Hancock, *J. Exp. Biol.* **32**, 802 (1955).
- [45] I. H. Riedel-Kruse, A. Hilfinger, J. Howard, and F. J'ulicher, *HFSP* **1**, 192 (2007).
- [46] F. Peruani, J. Starruß, V. Jakovljevic, L. Sjøgaard-Andersen, A. Deutsch, and M. Bär, *Phys. Rev. Lett.* **108**, 098102 (2012).
- [47] L. H. Cisneros, J. O. Kessler, S. Ganguly, and R. E. Goldstein, *Phys. Rev. E* **83**, 061907 (2011).
- [48] H. D. M. Moore, K. Dvořáková, N. Jenkins and W. G. Breed, *Nature* **418**, 174 (2002).
- [49] R. Kapral, *Adv. Chem. Phys.* **140**, 89 (2008).
- [50] G. Gompper, T. Ihle, D. M. Kroll, and R. G. Winkler, *Adv. Polym. Sci.* **221**, 1 (2009).
- [51] U. B. Kaupp, J. Solzin, E. Hildebrand, J. E. Brown, A. Helbig, V. Hagen, M. Beyermann, F. Pampaloni, and I. Weyand, *Nature Cell Biol.* **5**, 109 (2003).
- [52] For the flagellum model, we chose the parameters $l_0 = 0.5a$, $N_f = 100$, monomer mass $m_f = 10m$, $k = 2 \times 10^5 k_B T / a^2$, $\kappa = 10^4 k_B T / a^2$, $A = 0.2/a$, and $q = 4\pi / N_f l_0$. Volume exclusion is obtained by a repulsive Lennard-Jones potential with $\epsilon = 15k_B T$ and $r_0 = a$.
- [53] For Brownian Dynamics simulations with anisotropic friction (AF), the friction coefficients are chosen to be $\gamma_{\perp} = 10.0$ and $\gamma_{\parallel} = 16.8$, in order to reproduce the single-flagellum velocity $v_{f,0} / a f_0 \approx 2.75$ in MPC fluid when $c_0 l_0 = 0.02$.
- [54] The MPC fluid is governed by the side length a of the collision boxes, the mass m of the fluid particles, the thermal energy $k_B T$, the rotation angle $\alpha = 90^\circ$, and the average density of fluid particles $\rho_{MPC} = 10a^{-3}$. The natural time scale in MPC simulations is $\tau_0 = \sqrt{a^2 / (k_B T)}$. The collision time is $\Delta\tau / \tau_0 = 0.025$. With these parameters, the dynamic viscosity of the MPC fluid is given by $\eta = 3.02 \sqrt{a^2 (k_B T) / m}$ [49, 50].
- [55] See Supplemental Material at [URL by publisher] for movies of vortex arrays of circle SPPs and swimming flagella.
- [56] I. H. Riedel-Kruse, private communication (2013).